Modeling curvature-resisting material surfaces with isogeometric analysis

Animesh Rastogi[a], Berkin Dortdivanlioglu[a,b,*]

[a] *Civil, Architectural and Environmental Engineering, The University of Texas at Austin, Austin, 78712, TX, USA*
[b] *Oden Institute for Computational Engineering and Sciences, The University of Texas at Austin, Austin, 78712, TX, USA*

Abstract

Improved understanding of solid surface energy and its role in the overall mechanical properties is of great interest due to the emerging manufacturing techniques of nanostructures, coatings, and synthetic/biological bilayer-polymer hybrids. Continuum numerical modeling of surface stresses efficiently incorporates a zero-thickness membrane bonded to a bulk, intrinsically accounting for surface tension and surface elasticity. Compressive surface stresses are not possible in a purely membrane formulation, ignoring the surface flexural resistance. The extension of material surfaces to account for flexural resistance, i.e., the Steigmann–Ogden model, requires spatial derivatives of second order, posing significant challenges to standard discretization techniques. Hence, the effect of surface curvature resistance on the overall mechanical behavior of complex geometries remains elusive. Here, we develop a three-dimensional computational formulation of curvature-dependent surface energetics at finite strains using surface-enriched isogeometric analysis. Coupled with a hyperelastic bulk, bending-resistance of material surfaces furnishes a new physical length scale, i.e., the elastobending length. We quantify the effect of elastobending deformations for several numerical examples involving soft materials with thin coatings and liquid-shell surfaces, capturing budding-like behavior observed at cell membranes. Our results demonstrate a stiffer overall mechanical behavior when material surfaces resist bending deformations and illustrate how curvature effects lead to complex budding deformations at non-zero initial curvature states. The proposed methodology provides a robust computational foundation to help improve our understanding and mechanical characterization of soft solids, nanostructures, and biological membranes at small scales.

Keywords: surface curvature, isogeometric analysis, liquid shell, surface elasticity, size effects

1. Introduction

It is well established that physical properties and energy characteristics of materials' surfaces or interfaces differ from those of the encased bulk [1]. While the surface effects are negligible in stiff solids at macro scale, they significantly influence the mechanical response of nanostructures and soft solids at small scales (up to ∼mm). In soft solids such as gels, the surface energy (N/mm) is comparable with the bulk energy due to very low shear modulus (∼Pa), introducing a physical-length scale. The capillary forces and the resulting elastocapillary length-scale are critical for many physical phenomena such as elastowetting on soft solids [2–4], cavitation [5], and instabilities [6–8]. In stiff nanostructures, the surface-area-to-volume ratio is high, and therefore surface effects are pronounced, leading to size-dependent mechanical properties [9–12], surface piezoelectricity [13, 14], and pseudoelasticity [15, 16].

The majority of research on surface stresses in solids is based on Gurtin and Murdoch's continuum mechanics theory of surface elasticity[17]. Central to this theory is the idea that the solid surface is a two-dimensional membrane permanently attached to the bulk with its own thermodynamic structure. As a result, surface stresses and surface strains become energetically conjugate quantities. Steigmann and Ogden [18] generalized their theory to include surface flexural resistance by assuming that the surface energy depends on surface curvature along with in-plane surface strains. The surface cannot support compressive stresses if its flexural resistance is ignored [19]. This hinders comprehensive studies of complex surface phenomena such as bifurcations including global wrinkling [20–22] or

*Corresponding author.

localized crease instabilities [23, 24], triggered when compressive stresses on the boundary reach a critical threshold, for a very thin surface layer bonded to a substrate. Many theoretical, numerical, and experimental works have utilized the Gurtin–Murdoch [9–11, 25–29] and Steigmann–Ogden [12, 30–37] theories to quantify the effects of surface tension, surface elasticity (strain-dependent resistance to stretching) and surface curvature-resistance in the mechanical response of soft solids and nanostructures. From the computational standpoint, Yvonnett et al. [38] presented a finite element (FE) approach to model surface elasticity for two-dimensional small strain problems. Javili and Steinmann developed two- and three-dimensional FE frameworks that account for surface effects at finite strains [39, 40]. They later revised their framework by adopting a curvilinear-coordinate-based FE methodology for an efficient surface elasticity formulation [41]. He and Park recently presented a methodology to capture surface stresses that could easily be implemented in commercial FE softwares such as COMSOL and Ansys [42].

Most of the computational frameworks dealing with surface effects in solids ignore Steigmann and Ogden's extension to consider surface flexural resistance. The reason for this is that incorporating curvature-dependent surface energy in the current surface elasticity enhanced Galerkin FE models is challenging. The surface in the Steigmann–Ogden model is assumed to be a zero-thickness shell embedded in the three-dimensional space, necessitating a robust calculation of surface curvature. Surface curvature depends on second-order derivatives in space and therefore requires a surface representation with at-least C^1-continuity in the entire domain. The surface enrichment using the Lagrange basis function results in C^0-continuity across element boundaries. The C^1 continuous surface representation provided by Hermite basis functions is only limited to two-dimensional formulations. Isogeometric analysis (IGA), introduced by Hughes et al. [43] uses higher-order NURBS basis functions and facilitates the exact representation of curved geometries at the coarsest level of discretization. Furthermore, the same basis functions are used to construct the approximation of the field variable in the analysis. NURBS-based representation of the geometry allows C^k-continuity in the entire domain, giving IGA computational advantages over the standard finite element method to model higher-order problems. Consequently, IGA has emerged as a promising tool to solve geometric partial differential equations on surfaces [44, 45], model higher-order phase-field approximations [46–49], simulate the behavior of Kirchhoff–Love and Reissner—Mindlin shells through rotation-free formulations [50–59], and investigate curvature-mediated physics of biological cell membranes [60–64].

In this work, we leverage the advantages of isogeometric analysis and develop a three-dimensional computational framework to model curvature-resisting energetic surfaces in solids. Our framework can represent complex geometries, capture large deformations, and incorporate arbitrary nonlinear constitutive laws for the bulk and the surface. We first verify the framework by comparing it to an analytical solution at large deformations and then present several numerical examples elucidating the effects of surface curvature resistance in solids. Furthermore, we offer two examples to demonstrate how our framework can be used to model liquid-shell behavior on a hyperelastic bulk. The presented framework is generic and can be utilized to understand the behavior of artificially coated macroscopic solids, elucidate size-dependent properties of nanostructures, and investigate the curvature-mediated mechanical response of biological cell membranes or protocell membranes.

The manuscript is organized as follows. Section 2 gives the theoretical background and the computational implementation of the behavior of a solid encased by a zero-thickness curvature resisting surface. We begin with the kinematics of the problem in Section 2.1 followed by the constitutive laws used for the surface and the bulk in Section 2.2. We then present the variational equation suitable for computational implementation in Section 2.3. The computational framework is developed using isogeometric analysis. To this end, we briefly summarize the basics of the isogeometric analysis and how it is applied to discretize the variational equation in Section 2.4. In Section 3, we present several numerical examples and explore the physical aspects of curvature-dependent surface behavior in arbitrarily thick solids and bonded liquid shells. Finally, we conclude this work and provide an outlook for future work in Section 4.

2. Theory

The objective of this section is to establish the governing equations of solid-surface coupled mechanical behavior including surface curvature-resistance. The surface has zero-thickness and is endowed with its own thermodynamic structure distinct from the bulk. Following the Steigmann–Ogden theory, the surface flexural resistance is incorporated at the constitutive level along with surface tension and surface elasticity. The kinematic quantities including the surface

curvature are formulated in a curvilinear coordinate system which is directly suited for computational implementation using IGA.

2.1. Kinematics

Let us consider a solid bulk $\mathcal{B}$ in the three-dimensional space $\mathbb{R}^3$ occupying a reference configuration $\mathcal{B}_o$ at time $t = 0$ and a current configuration $\mathcal{B}_t$ at $t > 0$, as illustrated in Fig. 1. Let $\boldsymbol{\varphi}$ be the nonlinear deformation function that maps a material point $\boldsymbol{X}$ in the reference configuration to $\boldsymbol{x}$ in the current configuration as

$$\boldsymbol{x} = \boldsymbol{\varphi}(\boldsymbol{X}) \tag{1}$$

Let $\mathcal{S}_o = \partial\mathcal{B}_o$ and $\mathcal{S}_t = \partial\mathcal{B}_t$ denote the surface $\mathcal{S}$ of the bulk $\mathcal{B}$ in the reference and the current configurations, respectively. According to our convention, the surface quantities are represented as $\{\widehat{\bullet}\}$. The material points on the surface are labelled as $\widehat{\boldsymbol{X}}$ and $\widehat{\boldsymbol{x}}$ in the reference and the current configurations, respectively. Integral to the surface elasticity theory, the surface is assumed to be perfectly attached to the bulk at all configurations and therefore, its motion $\widehat{\boldsymbol{\varphi}}$ is convected by the bulk deformation map $\boldsymbol{\varphi}$. That is

$$\widehat{\boldsymbol{x}} = \widehat{\boldsymbol{\varphi}}(\widehat{\boldsymbol{X}}) \qquad \text{where} \qquad \widehat{\boldsymbol{\varphi}} = \boldsymbol{\varphi}|_{\partial\mathcal{B}_o} \tag{2}$$

The bulk material points $\boldsymbol{X}$ and $\boldsymbol{x}$ are represented in the standard Cartesian coordinate system. The bulk deformation gradient $\boldsymbol{F}$ is a linear function that relates an infinitesimal line element $d\boldsymbol{X} \in T\mathcal{B}_o$ in the reference configuration to its counterpart $d\boldsymbol{x} \in T\mathcal{B}_t$ in the current configuration through the relation $d\boldsymbol{x} = \boldsymbol{F} \cdot d\boldsymbol{X}$, where $\boldsymbol{F} = \text{Grad}\boldsymbol{x}$. The deformation gradient of the bulk $\boldsymbol{F}$ is rank-sufficient, and therefore, its inverse $\boldsymbol{f}$ exists, where $\boldsymbol{f} = \text{grad}\boldsymbol{x}$. The properties $\boldsymbol{f} \cdot \boldsymbol{F} = \boldsymbol{I}$ and $\boldsymbol{F} \cdot \boldsymbol{f} = \boldsymbol{i}$ hold where, $\boldsymbol{I}$ and $\boldsymbol{i}$ are the bulk identity tensors in the reference and the current configuration, respectively. The Jacobian of the bulk J is defined as the ratio of the volume element dv in the current and dV in the reference configuration and is given by $J = dv/dV = \det \boldsymbol{F}$. The surface $\mathcal{S}$ is a two-dimensional manifold embedded

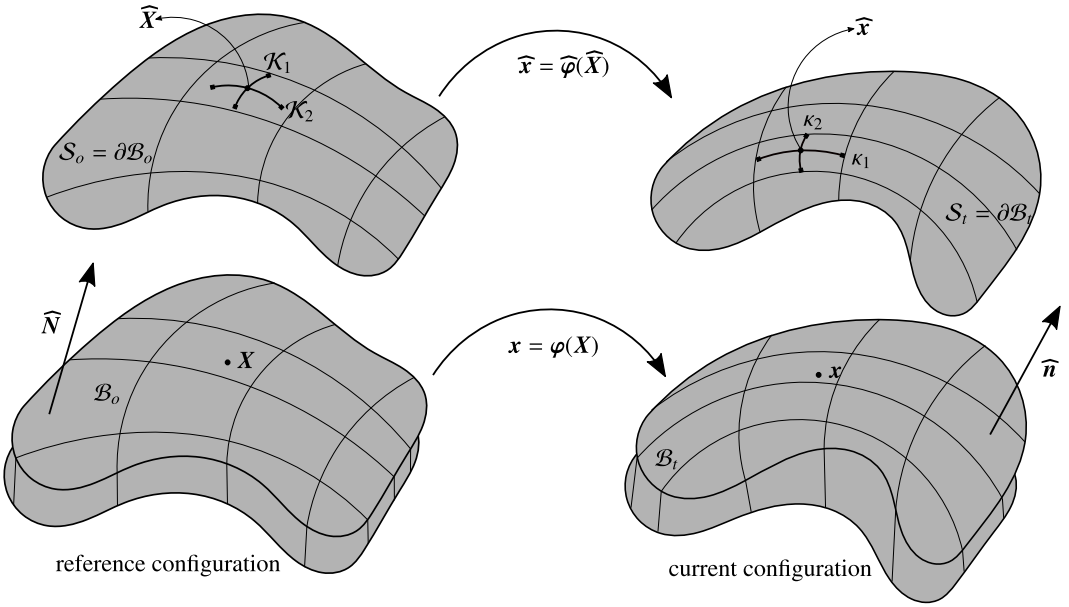

Figure 1: Finite deformation of the continuum body and its surface. The surface deformation is convected by the bulk deformation i.e. the surface is permanently attached to the bulk at all configurations. The curvature of the surface also changes as the body deforms.

in the three-dimensional space $\mathbb{R}^3$ and the surface material points $\widehat{\boldsymbol{X}}$ and $\widehat{\boldsymbol{x}}$ are parameterized locally by the curvilinear coordinates θ^α, where $\alpha \in \{1, 2\}$. With the curvilinear-coordinates parameterization, the covariant (natural) basis vectors for the tangent planes of the surfaces $\mathcal{S}_o$ and $\mathcal{S}_t$ are defined as

$$\widehat{\boldsymbol{G}}_\alpha = \widehat{\boldsymbol{X}}_{,\alpha} \qquad \text{and} \qquad \widehat{\boldsymbol{g}}_\alpha = \widehat{\boldsymbol{x}}_{,\alpha} \qquad \forall\alpha \in \{1,\, 2\} \tag{3}$$

where $\{\widehat{\cdot}\}_{,\alpha} = \partial\{\widehat{\cdot}\}/\partial\theta^{\alpha}$ is the partial derivative of a surface quantity with respect to the parametric coordinates θ^{α}. From the covariant basis vectors, follows the definition of unit normal vectors $\widehat{\boldsymbol{N}}$ and $\widehat{\boldsymbol{n}}$ on the surfaces $\mathcal{S}_o$ and $\mathcal{S}_t$. That is

$$\widehat{\boldsymbol{N}} = \frac{\widehat{\boldsymbol{G}}_1 \times \widehat{\boldsymbol{G}}_2}{\left\|\widehat{\boldsymbol{G}}_1 \times \widehat{\boldsymbol{G}}_2\right\|} \qquad \text{and} \qquad \widehat{\boldsymbol{n}} = \frac{\widehat{\boldsymbol{g}}_1 \times \widehat{\boldsymbol{g}}_2}{\left\|\widehat{\boldsymbol{g}}_1 \times \widehat{\boldsymbol{g}}_2\right\|} \tag{4}$$

The natural basis vectors $\widehat{\boldsymbol{G}}_{\alpha}$ and $\widehat{\boldsymbol{g}}_{\alpha}$ give rise to the covariant components of the metric tensor also known as the first fundamental form of the surface, which are expressed as

$$\widehat{G}_{\alpha\beta} = \widehat{\boldsymbol{G}}_{\alpha} \cdot \widehat{\boldsymbol{G}}_{\beta} \qquad \text{and} \qquad \widehat{g}_{\alpha\beta} = \widehat{\boldsymbol{g}}_{\alpha} \cdot \widehat{\boldsymbol{g}}_{\beta} \tag{5}$$

Geometrically, the first fundamental form determines the arc-length of a curve, angles between curves, and area of a region on the surface. The inverses $\widehat{G}^{\alpha\beta} = [\widehat{G}_{\alpha\beta}]^{-1}$ and $\widehat{g}^{\alpha\beta} = [\widehat{g}_{\alpha\beta}]^{-1}$ represent the contra-variant components of the metric tensor and define the associated contra-variant (dual) basis vectors of the surface as

$$\widehat{\boldsymbol{G}}^{\alpha} = \widehat{G}^{\alpha\beta}\,\widehat{\boldsymbol{G}}_{\beta} \qquad \text{and} \qquad \widehat{\boldsymbol{g}}^{\alpha} = \widehat{g}^{\alpha\beta}\,\widehat{\boldsymbol{g}}_{\beta} \tag{6}$$

Similar to the bulk, the surface deformation gradient $\widehat{\boldsymbol{F}}$ can be defined as a linear function which maps an infinitesimal line element $d\widehat{\boldsymbol{X}} \in T\mathcal{S}_o$ in the reference configuration to its counterpart $d\widehat{\boldsymbol{x}} \in T\mathcal{S}_t$ in the current configuration through the relation $d\widehat{\boldsymbol{x}} = \widehat{\boldsymbol{F}} \cdot d\widehat{\boldsymbol{X}}$, where $\widehat{\boldsymbol{F}} = \widehat{\text{Grad}\boldsymbol{x}} = \widehat{\boldsymbol{g}}_{\alpha} \otimes \widehat{\boldsymbol{G}}^{\alpha}$. Note that, in contrast to bulk, surface deformation gradient $\widehat{\boldsymbol{F}}$ is rank-deficient and therefore, its inverse $\widehat{\boldsymbol{f}}$ is given by the relation $\widehat{\boldsymbol{f}} = \widehat{\boldsymbol{G}}_{\alpha} \otimes \widehat{\boldsymbol{g}}^{\alpha}$. The surface Jacobian $\widehat{J}$ is defined as the ratio of the area element da in the current and dA in the reference configuration and is given by the relation $J = da/dA = |\widehat{\boldsymbol{g}}^1 \times \widehat{\boldsymbol{g}}^2 \| \widehat{\boldsymbol{G}}^1 \times \widehat{\boldsymbol{G}}^2|$. The right Cauchy-Green surface deformation tensor $\widehat{\boldsymbol{C}}$ and its inverse $\widehat{\boldsymbol{C}}^{-1}$ can now be defined using $\widehat{\boldsymbol{F}}$ and $\widehat{\boldsymbol{f}}$ as

$$\widehat{\boldsymbol{C}} = \widehat{\boldsymbol{F}}^T\,\widehat{\boldsymbol{F}} = \widehat{g}_{\alpha\beta}\widehat{\boldsymbol{G}}^{\alpha} \otimes \widehat{\boldsymbol{G}}^{\beta} \qquad \text{and} \qquad \widehat{\boldsymbol{C}}^{-1} = \widehat{\boldsymbol{f}}\,\widehat{\boldsymbol{f}}^T = \widehat{g}^{\alpha\beta}\widehat{\boldsymbol{G}}_{\alpha} \otimes \widehat{\boldsymbol{G}}_{\beta} \tag{7}$$

Next, we introduce the surface curvature tensor $\boldsymbol{b}$, represented using the second fundamental form $b_{\alpha\beta}$ of the surface as

$$\boldsymbol{b} = b_{\alpha\beta}\widehat{\boldsymbol{g}}^{\alpha} \otimes \widehat{\boldsymbol{g}}^{\beta} \qquad \text{where} \qquad b_{\alpha\beta} = \widehat{\boldsymbol{n}} \cdot \widehat{\boldsymbol{g}}_{\alpha,\beta} \tag{8}$$

Here $\widehat{\boldsymbol{g}}_{\alpha,\beta}$ is the parametric derivative of the tangent vector which depends on the second derivative of the surface position vector in the current configuration. Alternatively, the parametric derivative of the tangent vector can be written using the Gauss formulae [18] as

$$\widehat{\boldsymbol{g}}_{\alpha,\beta} = \widehat{\Gamma}^{\gamma}_{\alpha\beta}\widehat{\boldsymbol{g}}^{\gamma} + b_{\alpha\beta}\widehat{\boldsymbol{n}} \tag{9}$$

where, $\widehat{\Gamma}^{\gamma}_{\alpha\beta} = \widehat{\boldsymbol{g}}^{\gamma} \cdot \widehat{\boldsymbol{g}}_{\alpha,\beta}$ is the Christoffel symbol. Similarly, we can write the initial surface curvature tensor as

$$\boldsymbol{B} = B_{\alpha\beta}\widehat{\boldsymbol{G}}^{\alpha} \otimes \widehat{\boldsymbol{G}}^{\beta} \qquad \text{where} \qquad B_{\alpha\beta} = \widehat{\boldsymbol{N}} \cdot \widehat{\boldsymbol{G}}_{\alpha,\beta} \tag{10}$$

The principal curvatures κ_1 and κ_2 at a point on the surface is defined as the eigenvalues of the matrix

$$\widehat{g}^{\alpha\beta}b_{\beta\gamma} = \begin{bmatrix} \widehat{g}^{11} & \widehat{g}^{12} \\ \widehat{g}^{21} & \widehat{g}^{22} \end{bmatrix} \begin{bmatrix} b_{11} & b_{12} \\ b_{21} & b_{22} \end{bmatrix} \tag{11}$$

Physically, the principal curvatures are measures of how the surface bends in different directions. They are given by the maximum and minimum values of curvature at a point on the surface. The mean curvature H and the Gaussian curvature G of the surface are defined in terms of the invariants of the surface curvature tensor $\boldsymbol{b}$ as

$$H = \frac{1}{2}\,\text{tr}\,\boldsymbol{b} = \frac{1}{2}b_{\alpha\beta}\widehat{g}^{\alpha\beta} \quad \text{and} \quad G = \det\boldsymbol{b} = \frac{\det\left[b_{\alpha\beta}\right]}{\det\left[\widehat{g}_{\alpha\beta}\right]} \tag{12}$$

Finally, we define the relative curvature tensor $\boldsymbol{\kappa}$ [18, 35] and initial relative curvature tensor $\boldsymbol{\mathcal{K}}$ as

$$\boldsymbol{\kappa} = -\widehat{\boldsymbol{F}}^T \cdot \boldsymbol{b} \cdot \widehat{\boldsymbol{F}} = \kappa_{\alpha\beta}\widehat{\boldsymbol{G}}^{\alpha} \otimes \widehat{\boldsymbol{G}}^{\beta} \qquad \text{and} \qquad \boldsymbol{\mathcal{K}} = -\widehat{\boldsymbol{F}}^T \cdot \boldsymbol{B} \cdot \widehat{\boldsymbol{F}} = \mathcal{K}_{\alpha\beta}\widehat{\boldsymbol{G}}^{\alpha} \otimes \widehat{\boldsymbol{G}}^{\beta} \tag{13}$$

where $\kappa_{\alpha\beta}$ = -$b_{\alpha\beta}$ and $\mathcal{K}_{\alpha\beta}$ = -$B_{\alpha\beta}$. $\boldsymbol{\kappa}$ and $\boldsymbol{\mathcal{K}}$ are the counterparts of $\boldsymbol{b}$ and $\boldsymbol{B}$ respectively in the reference configuration.

2.2. Strain Energy and the Constitutive Law

The mechanical response of the solid encased by curvature-resisting energetic surface is described by the internal; strain energy function W_{int} with contributions from both the bulk and the surface. That is

$$W_{int} = \int_{\mathcal{B}_o} \phi \, dV + \int_{\partial\mathcal{B}_o} \widehat{\phi} \, dA \tag{14}$$

where, ϕ and $\widehat{\phi}$ are the internal strain energy functions per unit volume and per unit area for the bulk and the surface, respectively.

The bulk is assumed to be an isotropic neo-Hookean material for which the strain energy density function ϕ in the reference configuration is written as

$$\phi(\mathbf{C}) = \frac{\mu}{2}(\mathrm{tr}(\mathbf{C}) - 3) + \frac{\lambda}{4}\left(J^2 - 1\right) - \left(\frac{\lambda}{2} + \mu\right)\ln(J) \tag{15}$$

where, λ and μ are the Lamé parameters. The corresponding second Piola-Kirchhoff stress tensor $\boldsymbol{S}$ takes the following expression

$$\mathbf{S} = 2\frac{\partial\phi}{\partial\boldsymbol{C}} = \frac{\lambda}{2}\left(J^2 - 1\right)\mathbf{C}^{-1} + \mu\left(\mathbf{I} - \mathbf{C}^{-1}\right) \tag{16}$$

Following the Steigmann–Ogden theory, the surface constitutive law is assumed to have dependence on the in-plane resistance to deformation represented as well as resistance to the change in its curvature. The surface energy density function is therefore a function of the right Cauchy-Green deformation tensor $\widehat{\boldsymbol{C}}$ and the relative curvature tensor of the surface $\boldsymbol{\kappa}$. Furthermore, if the surface is orientable and isotropic [18, 35, 65], the surface energy density function $\widehat{\phi}$ is expressible as a function of six surface invariants $\{\widehat{I}_1, \widehat{I}_2, \widehat{I}_3, \widehat{I}_4, \widehat{I}_5, \widehat{I}_6\}$ as

$$\widehat{\phi}(\widehat{\boldsymbol{C}}, \boldsymbol{\kappa}) = \widehat{\phi}(\widehat{I}_1, \widehat{I}_2, \widehat{I}_3, \widehat{I}_4, \widehat{I}_5, \widehat{I}_6) \tag{17}$$

where, the six invariants are defined as

$$\begin{aligned} &\widehat{I}_1 = \mathrm{tr}\,\widehat{\boldsymbol{C}} \qquad \widehat{I}_2 = \det\widehat{\boldsymbol{C}} \qquad \widehat{I}_3 = \mathrm{tr}\,\boldsymbol{\kappa} \\ &\widehat{I}_4 = \det\boldsymbol{\kappa} \qquad \widehat{I}_5 = \mathrm{tr}(\widehat{\boldsymbol{C}}\boldsymbol{\kappa}) \qquad \widehat{I}_6 = \mathrm{tr}(\widehat{\boldsymbol{C}}\boldsymbol{\kappa}\widehat{\boldsymbol{\mu}}) \end{aligned} \tag{18}$$

Here, $\widehat{\boldsymbol{\mu}} = \widehat{\mu}^{\alpha\beta}\widehat{\boldsymbol{G}}_\alpha \otimes \widehat{\boldsymbol{G}}_\beta$ is the permutation tensor-density [18] with its components $\widehat{\mu}^{\alpha\beta}$ defined as

$$\widehat{\mu}^{11} = \widehat{\mu}^{22} = 0 \qquad \widehat{\mu}^{12} = -\widehat{\mu}^{21} = \sqrt{\det\left[\widehat{G}_{\alpha\beta}\right]} \tag{19}$$

In this work, we use a simple surface strain energy density function for the surface that captures the surface tension and surface elasticity via the first and second invariants $\widehat{I}_1$ and $\widehat{I}_2$. The surface curvature resistance is incorporated by penalizing the change in the third invariant $\widehat{I}_3 = \mathrm{tr}\,\boldsymbol{\kappa}$. That is

$$\widehat{\phi}(\widehat{\boldsymbol{C}}, \boldsymbol{\kappa}) = \underbrace{\widehat{\gamma}\widehat{J}}_{\text{surface tension}} + \underbrace{\frac{1}{2}\widehat{\lambda}\ln^2(\widehat{J}) + \frac{1}{2}\widehat{\mu}\left[\mathrm{tr}\left(\widehat{\boldsymbol{C}}\right) - 2 - 2\ln\left(\widehat{J}\right)\right]}_{\text{surface elasticity}} + \underbrace{\frac{1}{2}k_s(\mathrm{tr}\,\boldsymbol{\kappa} - \mathrm{tr}\,\boldsymbol{\mathcal{K}})^2}_{\text{surface curvature-resistance}} \tag{20}$$

where, $\widehat{\gamma}$ $[N/m]$ is the constant and isotropic surface tension, $\widehat{\lambda}$ $[N/m]$ and $\widehat{\mu}$ $[N/m]$ are the surface Lamé parameters, and k_s $[N/m^2]$ is the surface bending stiffness. Similar to bulk, the second Piola–Kirchhoff stress tensor for the surface thus becomes

$$\widehat{\boldsymbol{S}} = 2\frac{\partial\widehat{\phi}}{\partial\widehat{\boldsymbol{C}}} = \widehat{\lambda}\ln\left(\widehat{J}\right)\widehat{\boldsymbol{C}}^{-1} + \widehat{\mu}\left[\widehat{\boldsymbol{I}} - \widehat{\boldsymbol{C}}^{-1}\right] + \widehat{\gamma}\widehat{J}\,\widehat{\boldsymbol{C}}^{-1} \tag{21}$$

Due to surface curvature-resistance, a moment will be generated in the surface which is given by the expression

$$\widehat{\boldsymbol{M}} = \frac{\partial\widehat{\phi}}{\partial\boldsymbol{\kappa}} = k_s[\mathrm{tr}(\boldsymbol{\kappa}) - \mathrm{tr}(\boldsymbol{\mathcal{K}})]\widehat{\boldsymbol{I}} \tag{22}$$

The second Piola–Kirchhoff stress tensor and the moment tensor of the surface can also be expressed in curvilinear basis as follow

$$\widehat{\boldsymbol{S}} = \widehat{S}^{\alpha\beta}\widehat{\boldsymbol{G}}_\alpha \otimes \widehat{\boldsymbol{G}}_\beta \qquad \text{where} \qquad \widehat{S}^{\alpha\beta} = \widehat{\lambda}\ln\big(\widehat{J}\,\big)\widehat{g}^{\alpha\beta} + \widehat{\mu}\left[\widehat{G}^{\alpha\beta} - \widehat{g}^{\alpha\beta}\right] + \widehat{\gamma}\widehat{J}\widehat{g}^{\alpha\beta} \tag{23}$$

and

$$\widehat{\boldsymbol{M}} = \widehat{M}^{\alpha\beta}\widehat{\boldsymbol{G}}_\alpha \otimes \widehat{\boldsymbol{G}}_\beta \qquad \text{where} \qquad \widehat{M}^{\alpha\beta} = k_s\kappa_{\gamma\delta}\widehat{G}^{\gamma\delta}\widehat{G}^{\alpha\beta}\,, \tag{24}$$

respectively.

2.3. Total potential energy and the variational equation

To establish a computational framework, in this section, we derive the variational equation using the principle of minimization of the total potential energy. Let $\Pi = W_{int} + W_{ext}$ be the total potential energy of the system, where the total internal energy is given by Eq. (14). We assume dead loading in the system with a surface traction $\widehat{\boldsymbol{T}}$ in the reference configuration. The total external energy W_{ext} in the absence of body forces can thus be written as

$$W_{ext} = -\int_{\partial\mathcal{B}_o} \widehat{\boldsymbol{T}} \cdot \widehat{\boldsymbol{\varphi}}\, dA \tag{25}$$

The minimization of the total potential energy ($\delta\Pi = 0$), with respect to all admissible variations $\delta\boldsymbol{x} \in \mathcal{H}_0^1(\mathcal{B}_t)$ and $\delta\widehat{\boldsymbol{x}} \in \mathcal{H}_0^1(\mathcal{S}_t)$, renders the variational equation in the reference configuration as follow:

$$\int_{\mathcal{B}_o} \boldsymbol{S} : (\boldsymbol{F}^T \cdot \mathrm{Grad}\delta\boldsymbol{x})\, dV + \int_{\partial\mathcal{B}_o} [\widehat{\boldsymbol{T}}^{\,\alpha} \cdot \delta\widehat{\boldsymbol{g}}_\alpha + \widehat{\boldsymbol{M}}^{\,\alpha\beta} \cdot \delta\widehat{\boldsymbol{g}}_{\alpha,\beta}]\, dA - \int_{\partial\mathcal{B}_o} \widehat{\boldsymbol{T}} \cdot \delta\widehat{\boldsymbol{x}}\, dA = 0 \tag{26}$$

where $\widehat{\boldsymbol{T}}^{\,\alpha} = \widehat{S}^{\alpha\beta}\widehat{\boldsymbol{g}}_\beta + \widehat{M}^{\lambda\beta}\widehat{\Gamma}^{\,\alpha}_{\lambda\beta}\widehat{\boldsymbol{n}}$, $\widehat{\boldsymbol{M}}^{\,\alpha\beta} = -\widehat{M}^{\alpha\beta}\widehat{\boldsymbol{n}}$, $\delta\widehat{\boldsymbol{g}}_\alpha = \delta\widehat{\boldsymbol{x}}_{,\alpha}$, and $\delta\widehat{\boldsymbol{g}}_{\alpha,\beta} = \delta\widehat{\boldsymbol{x}}_{,\alpha\beta}$. Eq. (26) will now be discretized using isogeometric analysis in the next section.

2.4. Numerical implementation using isogeometric analysis

Non-Uniform Rational B-Splines (NURBS) basis functions are used to represent the bulk and the surface geometry as well as to discretize Eq. (26) in the context of isogeometric analysis. Here we provide a brief overview of B-splines and NURBS and how they are implemented to discretize the solid-surface coupled geometry and the associated kinematic quantities. Before defining B-spline functions, we need to define a knot vector. A knot vector, $\Xi = \{\xi_1, \xi_2, \ldots, \xi_{n+p+1}\}$, is a non-decreasing set of coordinates in the parameter space, where $\xi_i \in \mathbb{R}$ is the i^{th} knot, n is the number of basis functions, and p is the polynomial order. The knots in the knot vector partitions the parameter space into elements. With a knot vector Ξ, B-spline basis functions are defined recursively starting with zeroth-order ($p = 0$) basis function:

$$N_{i,0}(\xi) = \begin{cases} 1 & \text{if } \xi_i \le \xi < \xi_{i+1} \\ 0 & \text{otherwise} \end{cases} \tag{27}$$

Using the Cox-de Boor recursion algorithm, B-spline basis functions for $p \ge 1$ can be defined as

$$N_{i,p} = \frac{\xi - \xi_i}{\xi_{i+p} - \xi_i} N_{i,p-1}(\xi) + \frac{\xi_{i+p+1} - \xi}{\xi_{i+p+1} - \xi_{i+1}} \tag{28}$$

Given a set of B-spline basis functions $\{N_{i,p}\}_{i=1}^n$, a B-spline curve $\widetilde{\boldsymbol{\Omega}}$ can be constructed by taking its linear combination with the corresponding control points $\boldsymbol{P}_i \in \mathbb{R}^d$:

$$\widetilde{\boldsymbol{\Omega}}(\xi) = \sum_{i=1}^{n} N_{i,p}(\xi)\boldsymbol{P}_i \tag{29}$$

A B-spline surface, $\widehat{\boldsymbol{\Omega}}$ can be constructed by taking tensor product of two B-spline curves of polynomial orders p and q, and knot vectors $\Xi = \{\xi_1, \xi_2, \ldots, \xi_{n+p+1}\}$ and $\mathcal{H} = \{\eta_1, \eta_2, \ldots, \eta_{m+q+1}\}$ respectively:

$$\widehat{\boldsymbol{\Omega}}(\xi, \eta) = \sum_{i=1}^{n} \sum_{j=1}^{m} N_{i,p}(\xi) M_{j,q}(\eta) \boldsymbol{B}_{i,j} \tag{30}$$

Similarly, a B-spline solid $\boldsymbol{\Omega}$ can be constructed using an additional B-spline curve of polynomial order r with knot vector $\mathcal{Z} = \{\zeta_1, \zeta_2, \ldots, \zeta_{l+r+1}\}$:

$$\boldsymbol{\Omega}(\xi, \eta, \zeta) = \sum_{i=1}^{n} \sum_{j=1}^{m} \sum_{k=1}^{l} N_{i,p}(\xi) M_{j,q}(\eta) L_{k,r}(\zeta) \boldsymbol{B}_{i,j,k} \tag{31}$$

Non-Uniform Rational B-Splines (NURBS) are generalization of B-splines which give us the capability to exactly represent many complex geometries which can not be represented using B-splines. NURBS basis function in $\mathbb{R}^d$ is constructed by projecting a B-spline basis function in $\mathbb{R}^{d+1}$. This is obtained by associating a weight with each control points in B-splines

$$\widetilde{R}_i^p(\xi) = \frac{N_{i,p}(\xi) w_i}{W(\xi)} \tag{32}$$

where, w_i is the weight associated with the control point $\boldsymbol{B}_i$ and $W(\xi)$ is the weighting function defined as

$$W(\xi) = \sum_{i=1}^{n} N_{i,p}(\xi) w_i \tag{33}$$

We can write the basis functions for NURBS surface and solids by taking the tensor product of univariate NURBS basis function $\widetilde{R}_i^p(\xi)$ as

$$\begin{aligned} \widehat{\boldsymbol{R}}(\xi, \eta) &= \widetilde{R}_i^p(\xi) \otimes \widetilde{R}_i^q(\eta) \\ \boldsymbol{R}(\xi, \eta, \zeta) &= \widetilde{R}_i^p(\xi) \otimes \widetilde{R}_i^q(\eta) \otimes \widetilde{R}_i^r(\zeta) \end{aligned} \tag{34}$$

The bulk and the surface field variables can now be discretized using NURBS basis functions as

$$\begin{aligned} \boldsymbol{u}(\boldsymbol{\xi}) &= \sum_{a=1}^{N} N_a(\boldsymbol{\xi}) \boldsymbol{u}_a \quad \text{for the bulk} \\ \widehat{\boldsymbol{u}}(\widehat{\boldsymbol{\xi}}) &= \sum_{a=1}^{N} \widehat{N}_a(\widehat{\boldsymbol{\xi}}) \widehat{\boldsymbol{u}}_a \quad \text{for the surface} \end{aligned} \tag{35}$$

The integrals in Eq. (26) can be discretized and written as the internal and external residual vectors which will be collectively assembled in the global residual vector denoted by $\mathbb{R}$. The nonlinear system of governing equations are obtained by setting $\mathbb{R} = \mathbb{O}$, which is solved via an iterative Newton–Raphson scheme. To this end, consistent linearization of the resulting system of equations at any iteration k is established as

$$\mathbb{R}_{k+1} \stackrel{!}{=} \mathbb{0} \quad \text{with} \quad \mathbb{R}_{k+1} = \mathbb{R}_k + \mathbb{K}_k \cdot \Delta\mathbb{x}_k \quad \text{and} \quad \mathbb{K}_k := \left.\frac{\partial \mathbb{R}}{\partial \mathbb{x}}\right|_k \tag{36}$$

where, $\mathbb{K}_k$ is the tangent matrix at the kth iteration and $\mathbb{x}$ is the global deformation which consists of the deformations at all the control points. The global deformation vector $\mathbb{x}$ is updated at each iteration as $\mathbb{x}_{k+1} = \mathbb{x}_k + \Delta\mathbb{x}_k$, where the deformation update $\Delta\mathbb{x}$ is computed at the kth iteration from Eq. (36). The iterative process is stopped when the norm of the residual vector $\mathbb{R}$ numerically vanishes. For numerical integration, we adopt $(p+1) \times (q+1)$ and $(p+1) \times (q+1) \times (r+1)$ Gauss integration points for the surface and the bulk elements, respectively.

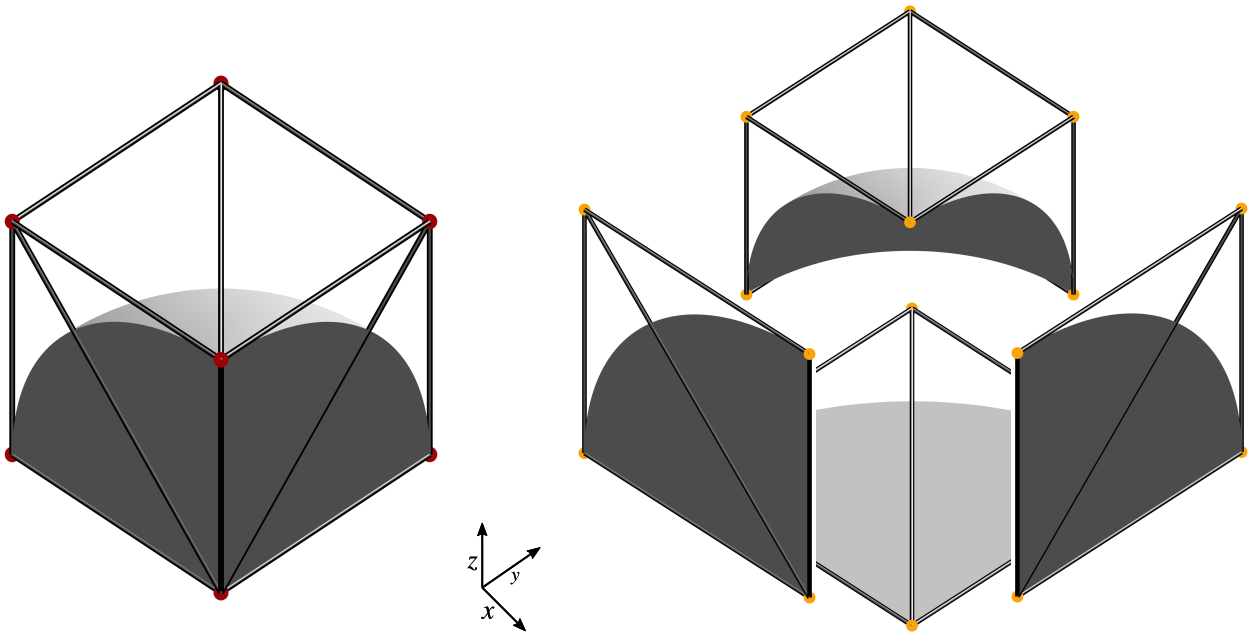

Bulk control net Surface control net

Figure 2: An illustration of partitioning of surfaces from volume mesh. The bulk and surface discretization overlap with each other. Therefore, each surface shares the control points corresponding to each face of the volume mesh

3. Numerical examples

We now present a variety of numerical examples to demonstrate the robustness of our framework developed in Section 2. The bulk, for all the examples, is made up of compressible neo-Hookean material with Lamé parameters λ and μ. The surfaces enclosing the bulk possess a surface energy which can have surface tension ($\widehat{\gamma}$), resistance to in-plane deformations ($\widehat{\mu}$ and $\widehat{\lambda}$), or resistance to change in their curvature (k_s). Our main emphasis in these examples is to elucidate the effects of surface curvature-resistance in the mechanics of solid-surface coupling. We define the normalized surface material parameters using bulk shear modulus μ and bulk thickness t. The dimensionless elasto-capillary, -stiffening, and -bending numbers [35] are defined as

$$\Gamma_{\widehat{\gamma}} = \frac{\widehat{\gamma}}{t\mu}, \qquad \Gamma_{\widehat{\mu}} = \frac{\widehat{\mu}}{t\mu}, \qquad \Gamma_{k_s} = \frac{k_s}{t^3\mu}, \tag{37}$$

respectively. The geometries are constructed using a single patch and the bulk and the surfaces are discretized with 3D and 2D NURBS elements respectively. Since the surfaces are assumed to be perfectly bonded to the bulk, their discretization overlap with each other. To *strongly* enforce rotational boundary conditions at the symmetric faces, we assign equal values to the degrees of freedom on the boundary and the degrees of freedom that are adjacent to the boundary [66, 67].

3.1. Radial compression of a thick-walled hollow sphere

In the first example, we verify our numerical framework with an analytical solution of a radially compressed thick-walled hollow sphere [18]. Fig. 3 shows the geometry and mesh for this example. The inner and the outer radius of the sphere are $A = 0.3$ *mm* and $B = 0.5$ *mm* respectively. The bulk material parameters are assumed to be $\mu = 1$ mN/mm^2 and $\lambda \approx 50000\mu$, which corresponds to the Poisson's ratio of $\nu = 0.4999$. An analytical solution is possible for this problem assuming the bulk behaves fully incompressible [18]. Accordingly, a high Poisson's ratio is set so as to approach the limit of incompressibility for comparisons with the analytical solution. We emphasize that analytical approaches for compressible bulk are in general not available in a closed form, further necessitating the

developed surface-enriched computational approach. The inner surface of the sphere is energetic and an external uniform pressure P is applied to its outer surface. Under the influence of the pressure P, the sphere uniformly compresses to an inner radius a and an outer radius b. The inner radial stretch is defined as $\lambda_a = a/A$ and holds the inequality $\lambda_a \leq 1$ for $P \geq 0$ because a decreases as the P increases. Due to the symmetry of the problem, we model one octant of the geometry. The geometry with the coarsest mesh is constructed with the knot vectors $\Xi = \{0, 0, 0, 1, 1, 1\}$, $\mathcal{H} = \{0, 0, 0, 1, 1, 1\}$, and $\mathcal{Z} = \{0, 0, 0, 1, 1, 1\}$ and quadratic polynomial order $p = q = r = 2$. We then order elevate the mesh to obtain a NURBS mesh with cubic polynomial order. Finally, we insert unique knot values at the desired locations, thus performing k-refinement to achieve the highest possible regularity over the domain and sufficiently fine mesh for accurate results. Based on the mesh convergence analysis, we choose 3125 cubic NURBS elements for the bulk and 625 cubic NURBS elements for the surface.

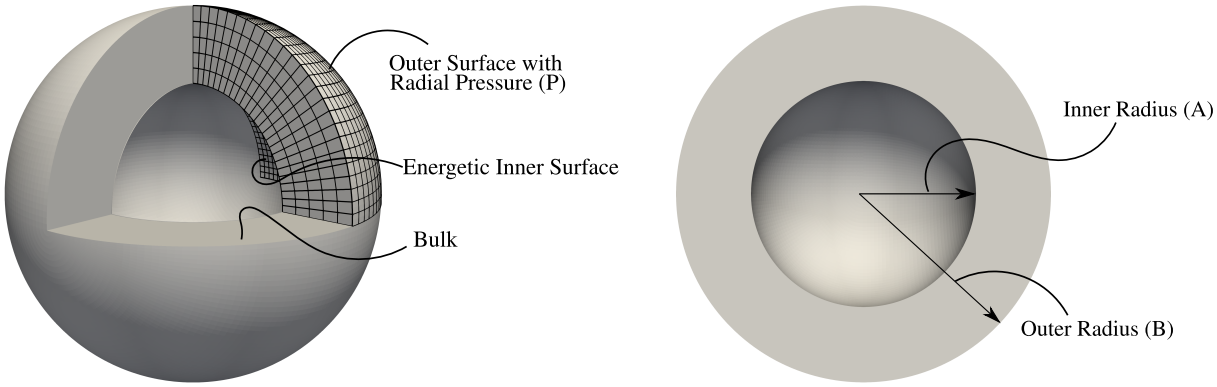

Figure 3: The geometry and NURBS mesh for the thick-walled hollow sphere. The inner surface is energetic and a pressure P is applied on the outer surface.

First, we compare our numerical results with the existing analytical solution [18] by plotting the variation of inner radial stretch λ_a with the normalized pressure $\overline{P} = P/\mu$ for different values of elasto-bending numbers Γ_{k_s}, see Fig. 4. We consider two cases for our model verification. Case 1, as shown in Fig. 4 A, presents the comparison between the numerical and analytical solutions without surface tension and surface elasticity. In case 2 (Fig. 4 B), we compare the numerical and analytical solutions in the presence of surface tension and surface elasticity. The analytical solution is presented in Appendix Appendix A. *The results show that the numerical results closely match the analytical results for both cases*. We observe that in case 1, λ_a starts with a value 1, while in case 2, it starts with 0.98. This deviation is due to the presence of surface tension in case B which reduces the surface-to-volume ratio to minimize the energy even in the absence of external pressure.

In Fig. 4, we observe that λ_a achieves a lower value for a particular pressure P on increasing Γ_{k_s}. This indicates that surface curvature resistance has a stiffening effect on the overall deformations of the sphere. To investigate this behavior further, we plot the variation of inner radial stretch λ_a against the elasto-bending number Γ_{k_s} for different values of elasto-stiffening number $\Gamma_{\widehat{\mu}}$, see Fig. 5. Due to the radial compression of the sphere, its inner radius a decreases, and therefore, *the curvature of the inner surface changes*. The surface bending energy thus competes with the bulk energy by penalizing the change in the inner surface curvature. Initially, for small values of Γ_{k_s}, λ_a almost remains the same as the case when $\Gamma_{k_s=0}$. This is because the surface bending energy is negligible in comparison to the bulk energy, and therefore does not penalize the change in the inner surface curvature. *As we increase Γ_{k_s} further, the surface bending energy becomes comparable to the bulk energy and as a result, a considerable surface moment is generated as curvature change is penalized. Consequently, the radial deformation significantly reduces and we observe a sharp increase in λ_a*. For large values of Γ_{k_s}, the inner surface does not allow any change in its curvature. Since the inner surface is perfectly bonded to the bulk, λ_a approaches 1, and the radial deformation of the sphere becomes negligible. Finally, we note that for a particular Γ_{k_s}, λ_a increases on increasing $\Gamma_{\widehat{\mu}}$ indicating the stiffening effect due to surface elasticity.

Next, we show the effects of surface curvature-resistance on the effective in-plane compressive stress $\widehat{\Sigma}$ in the

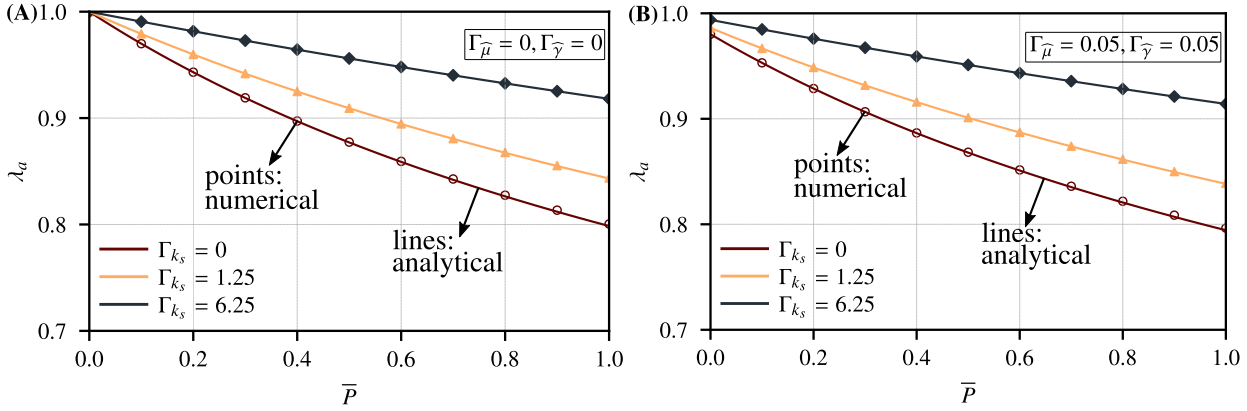

Figure 4: Inner radial stretch λ_a vs normalized pressure $\overline{P}$: (A) Without surface tension and surface elasticity. (B) With surface tension and surface elasticity. The numerical solutions closely match with the analytical solutions.

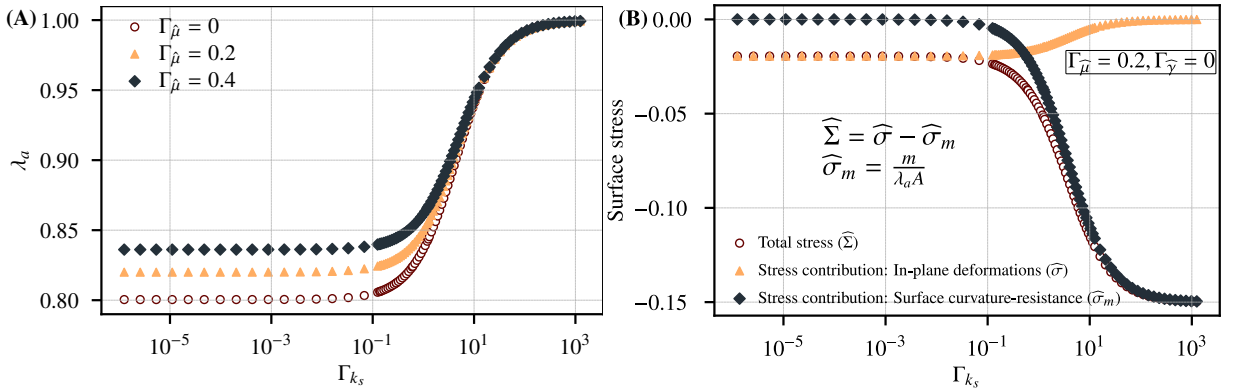

Figure 5: (A) Inner radial stretch λ_a vs elasto-bending number Γ_{k_s} for different elasto-stiffening numbers $\Gamma^{\widehat{\mu}}$. (B) Surface compressive stress ($\widehat{\Sigma}$) and its contributions from in-plane surface elasticity ($\widehat{\sigma}$) and surface curvature-resistance ($\widehat{\sigma}_m$) vs Γ_{k_s}.

inner surface, where $\widehat{\Sigma} = \widehat{\sigma} - \widehat{\sigma}_m$ (see Appendix Appendix A). In Fig. 5 B, we plot the effective in-plane compressive stress $\widehat{\Sigma}$ and its contributions from surface elasticity $\widehat{\sigma}$, and surface curvature-resistance $\widehat{\sigma}_m$ against the elasto-bending number Γ_{k_s}. The results show that till a particular value of Γ_{k_s}, $\widehat{\Sigma}$ coincides with $\widehat{\sigma}$, while $\widehat{\sigma}_m$ is negligible. This is because the contribution of the surface bending energy in the total potential energy is negligible in comparison to the bulk energy. However, there is considerable resistance to the inner surface compression due to surface elasticity and hence $\widehat{\sigma}$ coincides with the total compressive stress $\widehat{\Sigma}$. *As the surface bending stiffness increases further, the ability of the inner surface to resist the change in its curvature increases, and therefore the magnitudes of* $\widehat{\Sigma}$ *and* $\widehat{\sigma}_m$ *increase and approach the same value*. On the other hand, even in the presence of surface elasticity, the magnitude of $\widehat{\sigma}$ reduces to zero. This is because, as the surface curvature resistance increases, radial compression of the inner surface reduces, and therefore, the in-plane deformations of the inner surface decrease and vanish (see Fig. 5 A).

3.2. Deflection of a soft circular disc with surface energy

In this example, we explore the influence of curvature-resisting surfaces on the deflection of a thick soft circular disc under uniform loading. Fig. 6 shows the geometry and the boundary conditions of the disc. The disc has a radius $R = 0.5\ mm$, thickness $t = 0.1\ mm$ and is loaded uniformly over its upper surface with a load intensity $P = 0.3\ mN/mm^2$. The bulk possess a shear modulus $\mu = 1\ mN/mm^2$ and a bulk modulus $\lambda \approx 50000\mu$. The top and the bottom surface of the disc is endowed with surface energy.

First, we perform a mesh convergence study for the normalized tip deflection $\overline{w} = w/t$ and elasto-bending number $\Gamma_{k_s} = 5$. We start with the coarsest mesh (single element) constructed using the knot vectors $\Xi = \{0, 0, 0, 1, 1, 1\}$, $\mathcal{H} = \{0, 0, 0, 1, 1, 1\}$, and $\mathcal{Z} = \{0, 0, 0, 1, 1, 1\}$ and quadratic polynomial order ($p = q = r = 2$). We note that since the

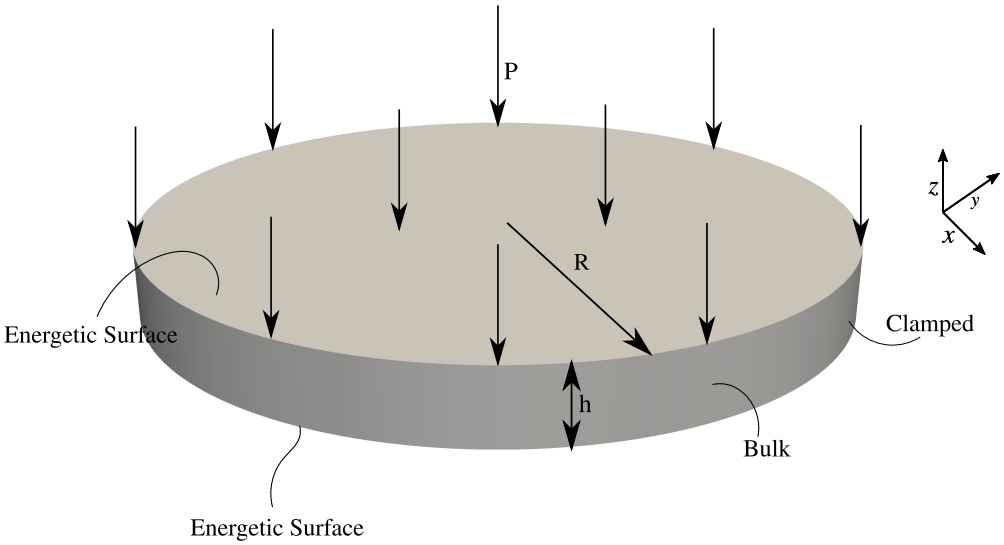

Figure 6: Geometry and boundary conditions for the thick circular disc.

geometry is curved, we need at-least quadratic polynomial order to accurately represent it using a single element. We perform order elevation (p-refinement) on the coarsest mesh to obtain NURBS mesh with cubic ($p = q = r = 3$) and quartic ($p = q = r = 4$) polynomial orders. We then perform h-refinement by inserting the knots at desired locations. The mesh convergence results are presented in Fig. 7 A. We observe a rapid convergence behavior for all the three cases of polynomial orders. A coarse mesh with only one element in the thickness direction (see Mesh 2 in Fig. 7 A) provides an accurate solution for both cubic and quartic polynomial orders.

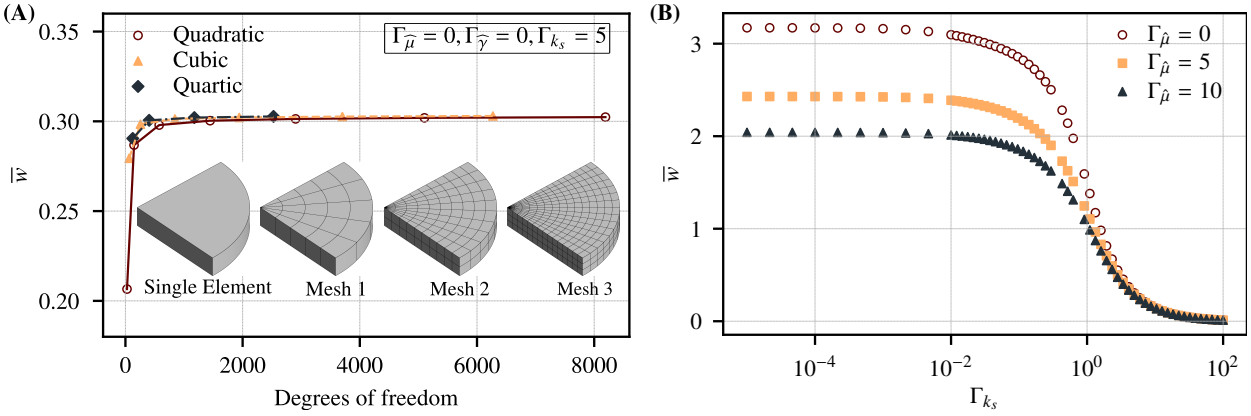

Figure 7: (A) Mesh convergence study of normalized tip deflection ($\overline{w}$) for $\Gamma_{k_s} = 5$. (B) Normalized tip-deflection $\overline{w}$ vs elasto-bending number Γ_{k_s} for different elasto-stiffening numbers $\Gamma_{\widehat{\mu}}$.

Next, we investigate the effects of surface bending stiffness on the deflection of the disc for different values of $\Gamma_{\widehat{\mu}}$. In Fig. 7 B, we plot the normalized tip deflection ($\overline{w}$) with the elasto-bending number (Γ_{k_s}). We make note of three regions in the plot and elucidate the effects of surface curvature resistance in each of these regions. In the first region, surface curvature resistance does not affect the deflection of the disc. This suggests that the bending energy is negligible in comparison to the bulk energy in the first region. In the second region, the deflection of the disc decreases rapidly and vanishes. This behavior suggests that a considerable amount of energy goes to change the curvature of the surfaces that would otherwise deflect the bulk of the disc. In the third region, surface-curvature resistance dominates the bulk energy, and hence the deflection in the disc is negligible on further increasing Γ_{k_s}. Finally, we note that the onset of each of the three regions is not affected by surface elasticity.

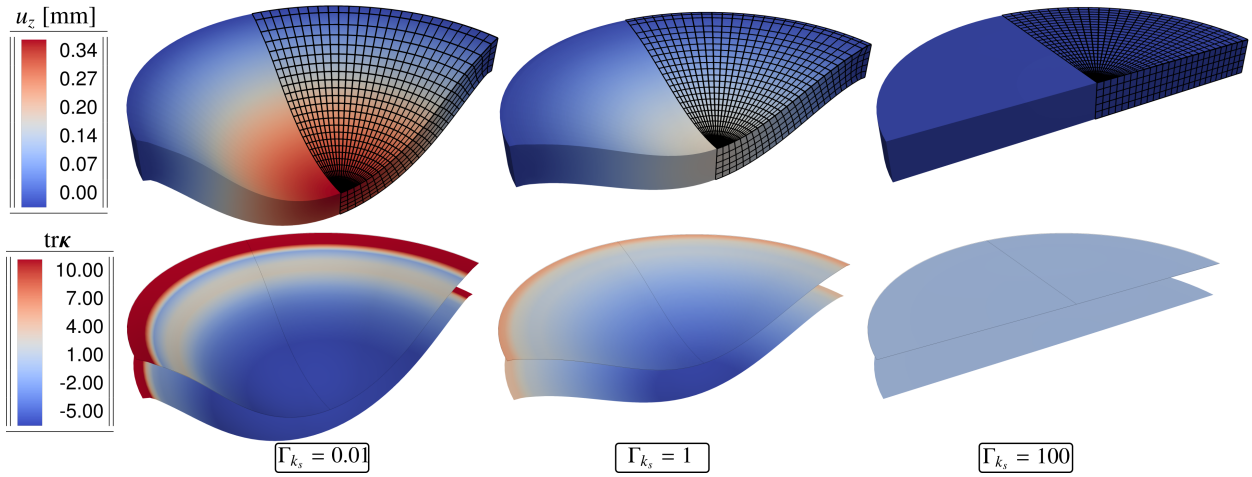

Figure 8: Deformation and the curvature contours of the deflection of the circular disc for different elasto-bending numbers Γ_{k_s}. Surface curvature-resistance reduces the deflection of the disc by penalizing the change in the surface curvature.

3.3. Pinching of a thin cylindrical tube

The above examples illustrated the coupled mechanical response of solids with surfaces that possess significant curvature resistance along with in-plane surface stresses. We now shift the focus and demonstrate how our framework can be used to model liquid-shell behavior, e.g., see [61, 68] using thin-shell kinematics without bulk effects. Liquid shells exhibit in-plane fluid-like behavior due to surface tension and out-of-plane solid-like behavior due to curvature resistance. An important example of a liquid shell is lipid bilayers that form the membrane of biological cells. Inspired by the mechanics of lipid bilayers, here we model a thin cylindrical tube whose ends are clamped and is pinched by a point load in its center. Fig. 9 shows the geometry, mesh, and boundary conditions for this example. The tube has a radius $R = 500\ \mu m$ and a small thickness $t = 10\ \mu m$. To mimic the liquid-shell-like behavior, we minimize the contribution of the bulk to the total energy of the system by choosing a fully compressible thin bulk with a small shear modulus $\mu = 0.01\ pN/\mu m^2$. Due to the point load, a *localized curvature* is induced in the surface of the cylinder which is penalized by a surface bending stiffness Γ_{k_s}. Due to symmetry, one-quarter of the geometry is used. To perform mesh convergence study, the coarsest NURBS mesh is constructed using the knot vectors $\Xi = \{0, 0, 0, 1, 1, 1\}$, $\mathcal{H} = \{0, 0, 0, 1, 1, 1\}$, and $\mathcal{Z} = \{0, 0, 0, 1, 1, 1\}$ and with quadratic polynomial order. During h-refinement, we globally refine the mesh near the area where the point load is applied to capture large deformations close to the point load. Based on the mesh convergence study, we choose a non-uniform quadratic mesh with 3636 elements in the bulk and 1848 elements on the surface as shown in Fig. 9.

Figure 10A-B show the deformation profiles of the cylinder around the line load for different Γ_{k_s} in the cross-sectional and longitudinal directions, respectively. We observe high curvature regions near the line load for the case without surface bending stiffness $\Gamma_{k_s} = 0$. *However, even a small value of surface bending stiffness ($\Gamma_{k_s} = 0.1$) supports the point load and regularizes the deformations*. On further increasing the surface bending stiffness, the deformations tend to smoothen out and reduce such that the high curvature regions are avoided.

The curvature-resisting behavior of thin cylindrical tube under point load as shown in Fig. 10 can be understood using the deformation and change in curvature ($\Delta\,\mathrm{tr}\,\boldsymbol{\kappa}$) contours around the line load, see Fig. 11. For the case when surface bending stiffness is small ($\Gamma_{k_s} = 0.1$), there is considerable amount of $\Delta\,\mathrm{tr}\,\boldsymbol{\kappa}$ around the line load. As we increase the surface bending stiffness, the ability of the surface to resist the change in its curvature increases, and therefore it tends to reduce the change in its curvature. Furthermore, when the surface bending stiffness is large, the surface does not allow any change in its curvature and therefore the deformations around the line load become negligible. Finally we note that, the quasi-static numerical solution of liquid shell behavior requires shear stabilization methods because of the absence of shear stiffness [53, 68]. In our model, however, the presence of bulk provides stabilization, and therefore does not require artificial shear stabilization methods.

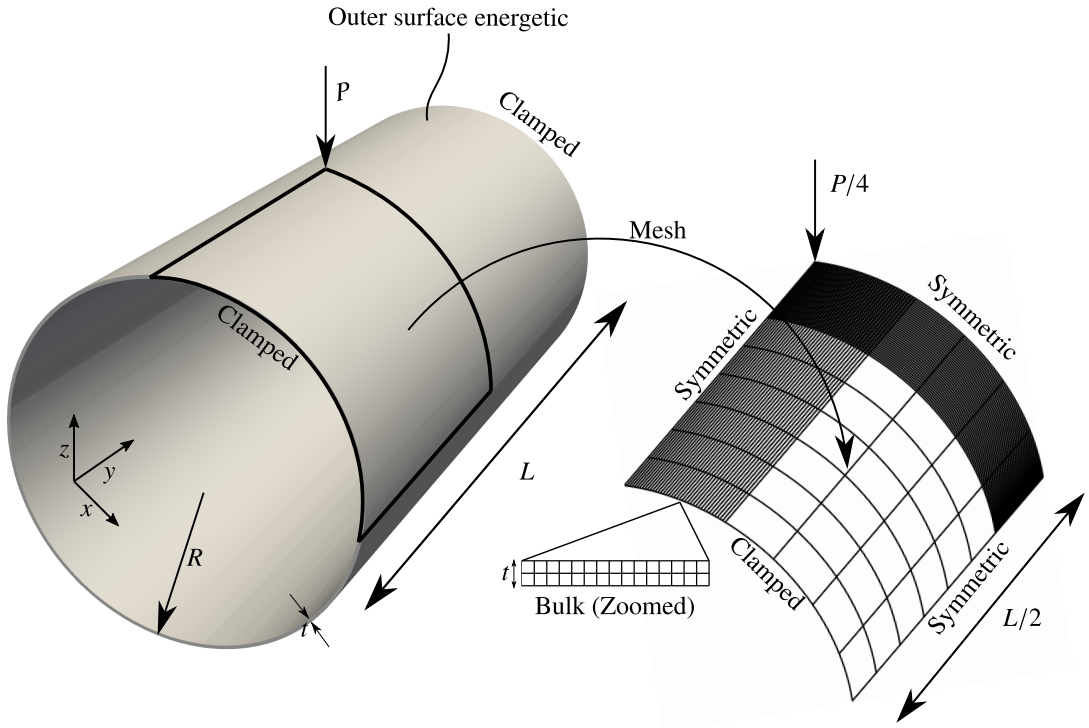

Figure 9: Geometry, mesh, and boundary conditions for the thin cylindrical tube encased by an energetic surface. The mesh is globally refined around the area where point load is applied to capture large deformations.

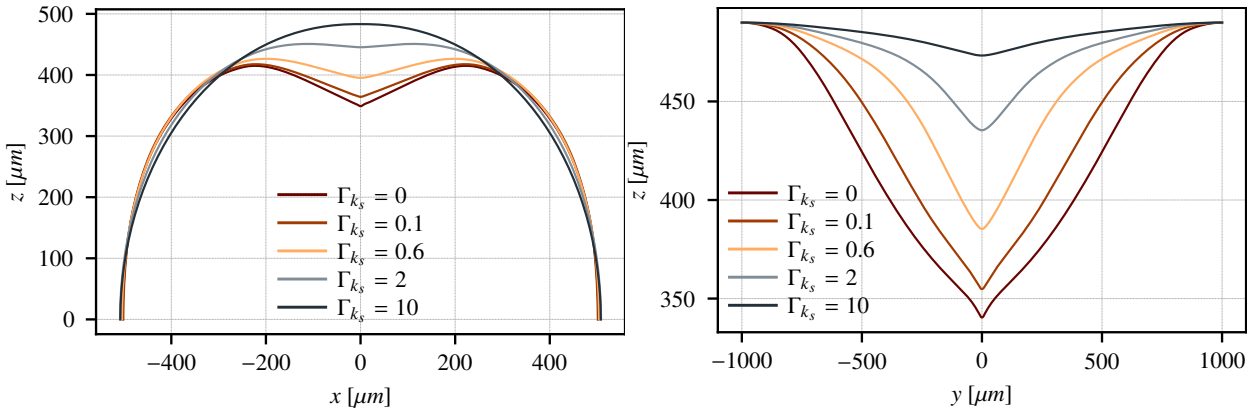

Figure 10: The membrane deformation profile in (A) cross-sectional direction and (B) longitudinal direction for different elasto-bending numbers Γ_{k_s}. The highly localized deformations are regularized due to the presence of surface curvature-resistance.

3.4. Budding of material surfaces

Our next example is inspired by the formation of cell membrane budding during the process of endocytosis. In particular, during endocytosis, coat proteins such as clathrin attach to a small area of the cell membrane and causes it to bend and form spherical shaped buds [69]. The driving force in this phenomenon is the protein-induced spontaneous curvature in the membrane that bends it into a positive or negative curvature based on the distribution of protein. Here, we model a zero-thickness liquid-shell as an energetic surface bonded to a fully compressible thin circular disc with radius $R = 5\ \mu m$, thickness $t = 0.025\ \mu m$ and shear modulus $\mu = 0.01\ pN/\mu m^2$. The top surface possess a surface tension $\Gamma_{\widetilde{\gamma}} = 0.4$ as well as surface curvature-resistance Γ_{k_s}. The spontaneous curvature due to the coat protein is modeled by assigning a non-zero $\mathrm{tr}\,\mathcal{K}$ to the surface bending energy in a small region of the surface. The area in the

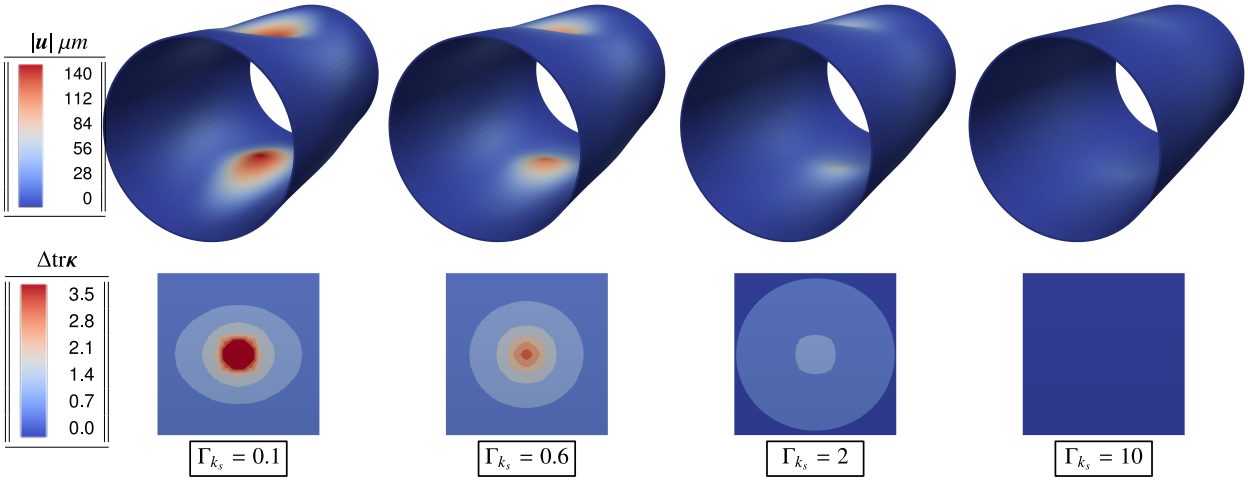

Figure 11: Deformation and curvature change contours for the pinching of thin cylindrical tube for different elasto-bending numbers Γ_{k_s}.

surface that represents coat protein posses a surface bending stiffness $\Gamma_{k_s} = 640$, while the rest of the surface possesses $\Gamma_{k_s} = 6.4$. Due to symmetry, we model a quarter of the disc geometry with 286 bulk and 286 surface elements. Both bulk and surface are discretized with quadratic C^1-continuous NURBS elements. The mesh is globally refined near the coated area to capture the sharp changes in curvature due to membrane bud formation.

We consider two different cases of membrane bud formation based on how coat proteins are distributed on the membrane, see Fig. 12. In case 1, the coat protein distribution exists in the region defined by the disc radius $0 \leq r \leq 1$ (orange) and $\mathrm{tr}\,\boldsymbol{\mathcal{K}}$ is assigned as

$$\mathrm{tr}\,\boldsymbol{\mathcal{K}} = \begin{cases} 15t & 0 \leq r \leq 1 \\ 0 & 1 < r \leq 5 \end{cases} \tag{38}$$

where $t \in [0, 10]$. For finite $\mathrm{tr}\,\boldsymbol{\mathcal{K}}$ values, a surface moment is generated which bends the orange colored area into a rounded bud shape. Next, in case 2, we model a heterogeneous distribution of proteins on the cell membrane leading to interesting bud formations. For example, in Fig. 12, the region defined by $0 \leq r \leq 1$ (orange) represents the coat protein which has a tendency to bend the membranes with a positive curvature. On the other hand, the region defined by $1 < r \leq 2$ (green) represents the coat protein bending the membranes with a negative curvature. $\mathrm{tr}\,\boldsymbol{\mathcal{K}}$ for case 2 is assigned as

$$\mathrm{tr}\,\boldsymbol{\mathcal{K}} = \begin{cases} 18t & 0 \leq r \leq 1 \\ -6t & 1 < r \leq 2 \\ 0 & 2 < r \leq 5 \end{cases} \tag{39}$$

Due to a negative $\mathrm{tr}\,\boldsymbol{\mathcal{K}}$ in the green-colored region, a negative surface moment is generated thus bending the membrane concave downwards. On the other hand, a positive $\mathrm{tr}\,\boldsymbol{\mathcal{K}}$ in the orange-colored region generates a positive moment thus bending the membrane concave upwards. Finally, we emphasize that along with providing shear stabilization to the numerical simulation as explained in Section 3.3, the bulk in our framework can also be used to model the effects of cytoskeleton forces during the membrane curvature generation.

4. Conclusion and future work

This paper presents a three-dimensional computational formulation to model curvature-resisting surfaces bonded to a soft bulk. The bulk formulation is general and can accommodate complex elastic and inelastic material models. On the boundary, we consider a zero-thickness surface that can resist curvature changes along with surface elasticity

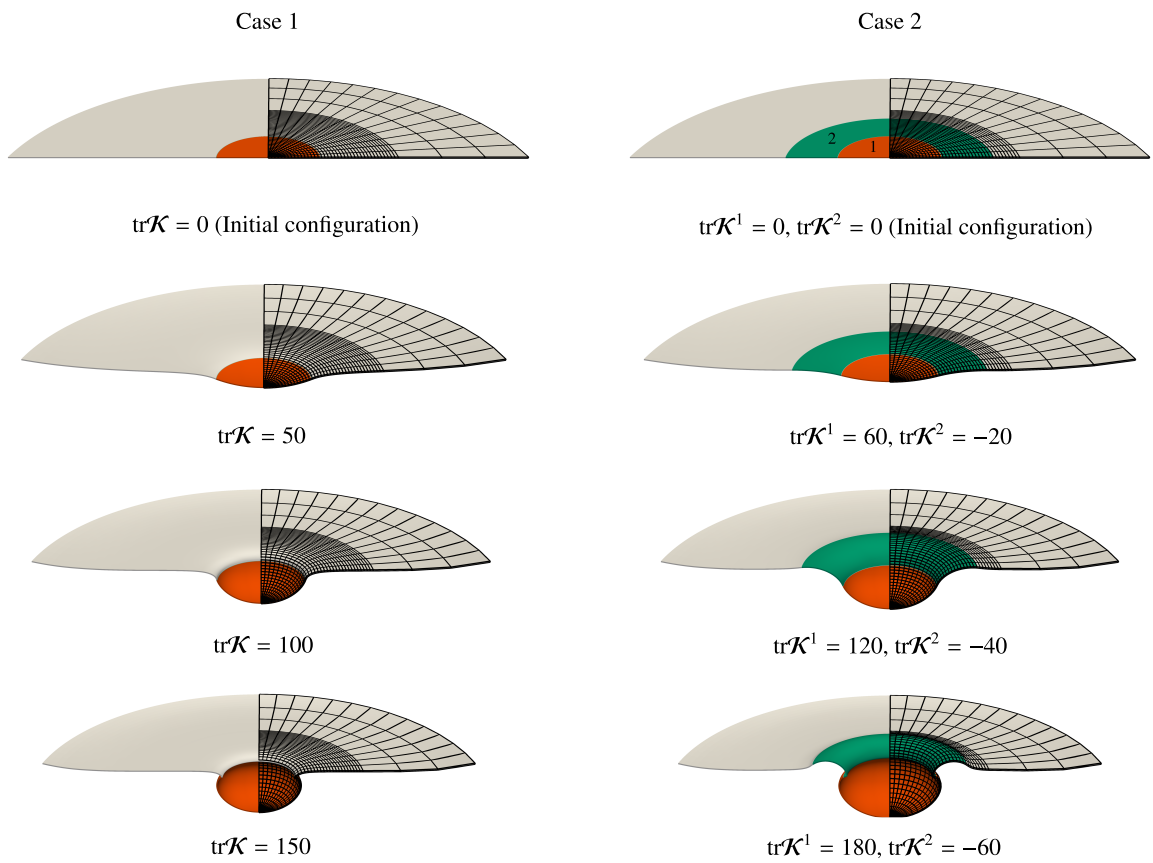

Figure 12: Formation of membrane budding depending on the distribution of coat protein on the membrane. The orange color in case 1 and orange and green colors in case 2 indicate the coat protein distribution. For case 2, indices 1 and 2 are used to represent the orange and the green colored region respectively.

and surface tension. The second-order dependence of surface curvature tensor in space is effectively addressed using at least C^1-continuous NURBS basis functions within the context of isogeometric analysis. The resulting higher order regularity also renders a numerical framework that is robust against locking effects, see Section 3.1 with the hollow sphere example. In this example, the results obtained closely match the analytical solution of the radially compressed thick-hollow sphere subjected to pressure for varying surface bending stiffnesses. Physical stiffness of energetic surfaces leads to an increased effective mechanical modulus of the overall structure, in balance with bulk effects. Due to the presence of bulk, a stable liquid-shell behavior is achieved and tested under distributed and point loading. The classical mesh localization issues that emerge in purely bulk formulations are resolved when curvature or surface effects are accounted for in the formulation. The last example shows the budding-like behavior of the surface when the local curvature properties, in particular, the initial stress-free curvature values are increased in parts of the computational domain. The evolution of final budded geometry is determined by competition between bending stiffness, surface elasticity and tension, and the bulk properties (shear modulus and the Poisson's ratio.) The developed computational tool is suitable to model thin-coated soft materials, biological and synthetic lipid membrane-polymer hybrids, and interface effects in nanostructures. Future work includes extending the current formulation to account for Helfrich-type curvature energetics suitable for lipid membranes [60–64], studying the effect of curvature-resistance on the Plateau-Rayleigh instabilities in solids [70, 71], and performing systematic studies to improve our quantitative understanding of surface effects in the mechanical characterization of soft materials using nano- and micro-indentation testing.

Acknowledgment

BD acknowledges funding from the National Science Foundation (NSF) through the DMREF program under grant number CMMI 2119716.

Appendix A. Analytical solution for compression of hollow sphere

In this appendix, we provide the analytical solution for the compression of a thick-hollow sphere with a curvature-resisting energetic inner surface. The generalized analytical solution for an incompressible hyperelastic bulk encased by a curvature-resisting energetic surface is given in [18]. Here, we present the solution specialized for the bulk and surface strain energy density functions mentioned in Section 2.2.

Let us consider a thick hollow spherical shell of inner radius A and outer radius B, uniformly compressed to an inner radius a and outer radius b by an external pressure P. Let λ_1, λ_2, and λ_3 be the principle stretches in the sphere in each direction. The bulk is incompressible, and therefore, the following relation hold for the principal stretches

$$\lambda_1 = \frac{1}{\lambda^2} \qquad \text{and} \qquad \lambda_2 = \lambda_3 = \lambda \tag{A.1}$$

The incompressible neo-Hookean constitutive model for the bulk is written as

$$\phi = \frac{\mu}{2}\,(\mathrm{tr}(\boldsymbol{C}) - 3) \tag{A.2}$$

where, $\mathrm{tr}(\boldsymbol{C})$ in terms of principal stretches can be written as

$$\mathrm{tr}(\boldsymbol{C}) = \lambda_1^2 + \lambda_2^2 + \lambda_3^2 = \frac{1}{\lambda^4} + 2\lambda^2 \tag{A.3}$$

The bulk strain energy density function $\phi(\lambda)$ thus becomes

$$\phi(\lambda) = \frac{\mu}{2}\left(\frac{1}{\lambda^4} + 2\lambda^2 - 3\right) \tag{A.4}$$

The surface strain energy density function is assumed to be

$$\widehat{\phi}(\widehat{\boldsymbol{C}}, \boldsymbol{\kappa}) = \widehat{\gamma}\widehat{J} + \frac{1}{2}\widehat{\lambda}\ln^2(\widehat{J}) + \frac{1}{2}\widehat{\mu}\left[\mathrm{tr}\left(\widehat{\boldsymbol{C}}\right) - 2 - 2\ln\left(\widehat{J}\right)\right] + \frac{1}{2}k_s(\mathrm{tr}\,\boldsymbol{\kappa} - \mathrm{tr}\,\boldsymbol{\mathcal{K}})^2 \tag{A.5}$$

where, $\mathrm{tr}\left(\widehat{\boldsymbol{C}}\right) = 2\lambda_a^2$, $\widehat{J} = \sqrt{det(\widehat{\boldsymbol{C}})} = \lambda_a^2$, $\mathrm{tr}\,\boldsymbol{\kappa} = -2A^{-1}\lambda_a$, and $\mathrm{tr}\,\boldsymbol{\mathcal{K}} = -2A^{-1}$.
The curvilinear components of the Cauchy stress tensor and surface moment tensor in the current configuration can then be given as

$$\widehat{\sigma}^{\alpha\beta} = \widehat{\sigma}\widehat{g}^{\alpha\beta} = \frac{1}{J}(\lambda_s \ln\left(\lambda_a^2\right) + \mu_s\lambda_a^2 - \mu_s + \gamma_s\lambda_a^2)\widehat{g}^{\alpha\beta} \qquad \text{and} \qquad m^{\alpha\beta} = m\widehat{g}^{\alpha\beta} = k_s(2A^{-1} - 2A^{-1}\lambda_a)\widehat{g}^{\alpha\beta} \tag{A.6}$$

The analytical solution is given by simultaneous solutions of the following three equations:

$$P = \frac{\mu}{2}\left(\frac{4\lambda_a^3 + 1}{\lambda_a^4} - \frac{4\lambda_b^3 + 1}{\lambda_b^4}\right)\lambda_b^2 - 2A^{-1}\lambda_a^{-1}\widehat{\Sigma}\lambda_b^2 \tag{A.7}$$

,

$$\widehat{\Sigma} = \widehat{\sigma} - \frac{m}{A\lambda_a} \tag{A.8}$$

$$\lambda_b = [1 + \left(\frac{A}{B}\right)^3 (\lambda_a^3 - 1)]^{1/3} \tag{A.9}$$

References

[1] A. W. Adamson, A. P. Gast, Physical Chemistry of Surfaces, 6th Edition, Wiley, New York, 1997.

[2] E. R. Jerison, Y. Xu, L. A. Wilen, E. R. Dufresne, Deformation of an Elastic Substrate by a Three-Phase Contact Line, Physical Review Letters 106 (2011) 186103. doi:10.1103/PhysRevLett.106.186103.

[3] R. W. Style, E. R. Dufresne, Static wetting on deformable substrates, from liquids to soft solids, Soft Matter 8 (2012) 7177. doi:10.1039/c2sm25540e.

[4] J. Dervaux, M. Roché, L. Limat, Nonlinear theory of wetting on deformable substrates, Soft Matter 16 (2020) 5157–5176. doi:10.1039/D0SM00395F.

[5] C. W. Barney, C. E. Dougan, K. R. McLeod, A. Kazemi-Moridani, Y. Zheng, Z. Ye, S. Tiwari, I. Sacligil, R. A. Riggleman, S. Cai, J.-H. Lee, S. R. Peyton, G. N. Tew, A. J. Crosby, Cavitation in soft matter, Proceedings of the National Academy of Sciences 117 (2020) 9157–9165.

[6] S. Mora, T. Phou, J.-M. Fromental, L. M. Pismen, Y. Pomeau, Capillarity Driven Instability of a Soft Solid, Physical Review Letters 105 (2010) 214301.

[7] S. Mora, M. Abkarian, H. Tabuteau, Y. Pomeau, Surface instability of soft solids under strain, Soft matter 7 (2011) 10612–10619.

[8] Q. Liu, T. Ouchi, L. Jin, R. Hayward, Z. Suo, Elastocapillary Crease, Physical Review Letters 122 (2019) 098003.

[9] R. E. Miller, V. B. Shenoy, Size-dependent elastic properties of nanosized structural elements, Nanotechnology 11 (2000) 139–147.

[10] G. Y. Jing, H. L. Duan, X. M. Sun, Z. S. Zhang, J. Xu, Y. D. Li, J. X. Wang, D. P. Yu, Surface effects on elastic properties of silver nanowires: Contact atomic-force microscopy, Physical Review B 73 (2006) 235409. doi:10.1103/PhysRevB.73.235409.

[11] J. Wang, Z. Huang, H. Duan, S. Yu, X. Feng, G. Wang, W. Zhang, T. Wang, Surface stress effect in mechanics of nanostructured materials, Acta Mechanica Solida Sinica 24 (2011) 52–82.

[12] P. Chhapadia, P. Mohammadi, P. Sharma, Curvature-dependent surface energy and implications for nanostructures, Journal of the Mechanics and Physics of Solids 59 (2011) 2103–2115.

[13] C. Li, W. Guo, Y. Kong, H. Gao, Size-dependent piezoelectricity in zinc oxide nanofilms from first-principles calculations, Applied Physics Letters 90 (2007) 033108.

[14] S. Dai, M. Gharbi, P. Sharma, H. S. Park, Surface piezoelectricity: Size effects in nanostructures and the emergence of piezoelectricity in non-piezoelectric materials, Journal of Applied Physics 110 (2011) 104305.

[15] W. Liang, M. Zhou, F. Ke, Shape Memory Effect in Cu Nanowires, Nano Letters 5 (2005) 2039–2043.

[16] H. S. Park, K. Gall, J. A. Zimmerman, Shape Memory and Pseudoelasticity in Metal Nanowires, Physical Review Letters 95 (2005) 255504.

[17] M. E. Gurtin, A. Ian Murdoch, A continuum theory of elastic material surfaces, Archive for Rational Mechanics and Analysis 57 (1975) 291–323.

[18] D. J. Steigmann, R. W. Ogden, Elastic surface—substrate interactions, Proceedings of the Royal Society of London. Series A: Mathematical, Physical and Engineering Sciences 455 (1999) 437–474.

[19] D. J. Steigmann, R. W. Ogden, Plane deformations of elastic solids with intrinsic boundary elasticity, Proceedings of the Royal Society of London. Series A: Mathematical, Physical and Engineering Sciences 453 (1997) 853–877. doi:10.1098/rspa.1997.0047.

[20] D. J. Steigmann, R. W. Ogden, A Necessary Condition for Energy-Minimizing Plane Deformations of Elastic Solids with Intrinsic Boundary Elasticity, Mathematics and Mechanics of Solids 2 (1997) 3–16. doi:10.1177/108128659700200101.

[21] B. Dortdivanlioglu, A. Javili, C. Linder, Computational aspects of morphological instabilities using isogeometric analysis, Computer Methods in Applied Mechanics and Engineering 316 (2017) 261–279.

[22] A. D. Bakiler, B. Dortdivanlioglu, A. Javili, From beams to bilayers: A unifying approach towards instabilities of compressible domains under plane deformations, International Journal of Non-Linear Mechanics 135 (2021) 103752. doi:10.1016/j.ijnonlinmec.2021.103752.

[23] E. Hohlfeld, L. Mahadevan, Unfolding the Sulcus, Physical Review Letters 106 (2011) 105702. doi:10.1103/PhysRevLett.106.105702.

[24] B. Dortdivanlioglu, N. E. D. Yilmaz, K. B. Goh, X. Zheng, C. Linder, Swelling-Induced Interface Crease Instabilities at Hydrogel Bilayers, Journal of Elasticity 145 (2021) 31–47. doi:10.1007/s10659-020-09810-8.

[25] Q. Xu, K. E. Jensen, R. Boltyanskiy, R. Sarfati, R. W. Style, E. R. Dufresne, Direct measurement of strain-dependent solid surface stress, Nature Communications 8 (2017) 555.

[26] S. Krichen, L. Liu, P. Sharma, Liquid inclusions in soft materials: Capillary effect, mechanical stiffening and enhanced electromechanical response, Journal of the Mechanics and Physics of Solids 127 (2019) 332–357. doi:10.1016/j.jmps.2019.03.010.

[27] C.-Y. Hui, Z. Liu, N. Bain, A. Jagota, E. R. Dufresne, R. W. Style, R. Kiyama, J. P. Gong, How surface stress transforms surface profiles and adhesion of rough elastic bodies, Proceedings of the Royal Society A: Mathematical, Physical and Engineering Sciences 476 (2020) 20200477.

[28] N. Bain, A. Jagota, K. Smith-Mannschott, S. Heyden, R. W. Style, E. R. Dufresne, Surface Tension and the Strain-Dependent Topography of Soft Solids, Physical Review Letters 127 (2021) 208001. doi:10.1103/PhysRevLett.127.208001.

[29] B. Dortdivanlioglu, A. Javili, Boundary viscoelasticity theory at finite deformations and computational implementation using isogeometric analysis, Computer Methods in Applied Mechanics and Engineering 374 (2021) 113579.

[30] A. Y. Zemlyanova, S. G. Mogilevskaya, On Spherical Inhomogeneity With Steigmann–Ogden Interface, Journal of Applied Mechanics 85 (2018).

[31] Z. Han, S. G. Mogilevskaya, D. Schillinger, Local fields and overall transverse properties of unidirectional composite materials with multiple nanofibers and Steigmann–Ogden interfaces, International Journal of Solids and Structures 147 (2018) 166–182. doi:10.1016/j.ijsolstr.2018.05.019.

[32] X. Li, C. Mi, Nanoindentation of a half-space due to a rigid cylindrical roller based on Steigmann–Ogden surface mechanical model, International Journal of Mechanics and Materials in Design 17 (2021) 25–40.

[33] C. Y. Hui, Z. Liu, A. Jagota, Effect of surface bending and stress on the transmission of line force to an elastic substrate, Proceedings of the Royal Society A: Mathematical, Physical and Engineering Sciences 474 (2018) 20170775.

[34] N. Lapinski, Z. Liu, S. Yang, C.-Y. Hui, A. Jagota, A surface with stress, extensional elasticity, and bending stiffness, Soft Matter 15 (2019) 3817–3827.

[35] Z. Liu, A. Jagota, C.-Y. Hui, Modeling of surface mechanical behaviors of soft elastic solids: theory and examples, Soft Matter 16 (2020) 6875–6889.
[36] S. G. Mogilevskaya, A. Y. Zemlyanova, V. I. Kushch, Fiber- and Particle-Reinforced Composite Materials With the Gurtin–Murdoch and Steigmann–Ogden Surface Energy Endowed Interfaces, Applied Mechanics Reviews 73 (2021) 050801. doi:10.1115/1.4051880.
[37] D. Neffati, Y. Kulkarni, Homogenization of Surface Energy and Elasticity for Highly Rough Surfaces, Journal of Applied Mechanics 89 (2022) 041004. doi:10.1115/1.4053081.
[38] J. Yvonnet, H. L. Quang, Q.-C. He, An xfem/level set approach to modelling surface/interface effects and to computing the size-dependent effective properties of nanocomposites, Computational Mechanics 42 (1) (2008) 119–131.
[39] A. Javili, P. Steinmann, A finite element framework for continua with boundary energies. Part I: The two-dimensional case, Computer Methods in Applied Mechanics and Engineering 198 (2009) 2198–2208.
[40] A. Javili, P. Steinmann, A finite element framework for continua with boundary energies. Part II: The three-dimensional case, Computer Methods in Applied Mechanics and Engineering 199 (2010) 755–765.
[41] A. Javili, A. McBride, P. Steinmann, B. D. Reddy, A unified computational framework for bulk and surface elasticity theory: a curvilinear-coordinate-based finite element methodology, Computational Mechanics 54 (2014) 745–762.
[42] J. He, H. S. Park, A methodology for modeling surface effects on stiff and soft solids, Computational Mechanics 61 (2018) 687–697.
[43] T. J. R. Hughes, J. A. Cottrell, Y. Bazilevs, Isogeometric analysis: CAD, finite elements, NURBS, exact geometry and mesh refinement, Computer Methods in Applied Mechanics and Engineering 194 (2005) 4135–4195.
[44] A. Bartezzaghi, L. Dedè, A. Quarteroni, Isogeometric Analysis of high order Partial Differential Equations on surfaces, Computer Methods in Applied Mechanics and Engineering 295 (2015) 446–469.
[45] A. Bartezzaghi, L. Dedè, A. Quarteroni, Isogeometric analysis of geometric partial differential equations, Computer Methods in Applied Mechanics and Engineering 311 (2016) 625–647.
[46] M. J. Borden, T. J. R. Hughes, C. M. Landis, C. V. Verhoosel, A higher-order phase-field model for brittle fracture: Formulation and analysis within the isogeometric analysis framework, Computer Methods in Applied Mechanics and Engineering 273 (2014) 100–118.
[47] M. Klassen, I. Muench, S. Klinkel, Phase field modeling with IGA and FEM: Error surveillance in the transition zone, PAMM 19 (2019) e201900167.
[48] D. Proserpio, M. Ambati, L. De Lorenzis, J. Kiendl, A framework for efficient isogeometric computations of phase-field brittle fracture in multipatch shell structures, Computer Methods in Applied Mechanics and Engineering 372 (2020) 113363.
[49] N. Valizadeh, Developments in Isogeometric Analysis and Application to High-Order Phase-Field Models of Biomembranes (2022).
[50] J. Kiendl, K. U. Bletzinger, J. Linhard, R. Wüchner, Isogeometric shell analysis with Kirchhoff–Love elements, Computer Methods in Applied Mechanics and Engineering 198 (2009) 3902–3914.
[51] J. Kiendl, Y. Bazilevs, M. C. Hsu, R. Wüchner, K. U. Bletzinger, The bending strip method for isogeometric analysis of Kirchhoff–Love shell structures comprised of multiple patches, Computer Methods in Applied Mechanics and Engineering 199 (2010) 2403–2416.
[52] A. P. Nagy, S. T. IJsselmuiden, M. M. Abdalla, Isogeometric design of anisotropic shells: Optimal form and material distribution, Computer Methods in Applied Mechanics and Engineering 264 (2013) 145–162.
[53] R. A. Sauer, T. X. Duong, C. J. Corbett, A computational formulation for constrained solid and liquid membranes considering isogeometric finite elements, Computer Methods in Applied Mechanics and Engineering 271 (2014) 48–68. doi:10.1016/j.cma.2013.11.025.
[54] T. X. Duong, F. Roohbakhshan, R. A. Sauer, A new rotation-free isogeometric thin shell formulation and a corresponding continuity constraint for patch boundaries, Computer Methods in Applied Mechanics and Engineering 316 (2017) 43–83.
[55] D. J. Benson, Y. Bazilevs, M. C. Hsu, T. J. R. Hughes, Isogeometric shell analysis: The Reissner–Mindlin shell, Computer Methods in Applied Mechanics and Engineering 199 (2010) 276–289.
[56] C. H. Thai, H. Nguyen-Xuan, N. Nguyen-Thanh, T.-H. Le, T. Nguyen-Thoi, T. Rabczuk, Static, free vibration, and buckling analysis of laminated composite Reissner–Mindlin plates using NURBS-based isogeometric approach, International Journal for Numerical Methods in Engineering 91 (2012) 571–603.
[57] W. Dornisch, S. Klinkel, B. Simeon, Isogeometric Reissner–Mindlin shell analysis with exactly calculated director vectors, Computer Methods in Applied Mechanics and Engineering 253 (2013) 491–504.
[58] P. Kang, S.-K. Youn, Isogeometric analysis of topologically complex shell structures, Finite Elements in Analysis and Design 99 (2015) 68–81.
[59] Z. Lei, F. Gillot, L. Jezequel, Developments of the mixed grid isogeometric Reissner–Mindlin shell: Serendipity basis and modified reduced quadrature, European Journal of Mechanics - A/Solids 54 (2015) 105–119.
[60] A. B. Tepole, H. Kabaria, K.-U. Bletzinger, E. Kuhl, Isogeometric Kirchhoff-Love shell formulations for biological membranes, Computer methods in applied mechanics and engineering 293 (2015) 328–347.
[61] R. A. Sauer, T. X. Duong, K. K. Mandadapu, D. J. Steigmann, A stabilized finite element formulation for liquid shells and its application to lipid bilayers, Journal of Computational Physics 330 (2017) 436–466.
[62] A. Bartezzaghi, L. Dedè, A. Quarteroni, Biomembrane modeling with isogeometric analysis, Computer Methods in Applied Mechanics and Engineering 347 (2019) 103–119.
[63] R. Vasan, S. Rudraraju, M. Akamatsu, K. Garikipati, P. Rangamani, A mechanical model reveals that non-axisymmetric buckling lowers the energy barrier associated with membrane neck constriction, Soft Matter 16 (2020) 784–797.
[64] D. Auddya, X. Zhang, R. Gulati, R. Vasan, K. Garikipati, P. Rangamani, S. Rudraraju, Biomembranes undergo complex, non-axisymmetric deformations governed by Kirchhoff–Love kinematicsand revealed by a three-dimensional computational framework, Proceedings of the Royal Society A: Mathematical, Physical and Engineering Sciences 477 (2021) 20210246.
[65] Q.-s. Zheng, Two-dimensional tensor function representation for all kinds of material symmetry, Proceedings of the Royal Society of London. Series A: Mathematical and Physical Sciences 443 (1993) 127–138.
[66] D. J. Benson, Y. Bazilevs, M. C. Hsu, T. J. R. Hughes, A large deformation, rotation-free, isogeometric shell, Computer Methods in Applied Mechanics and Engineering 200 (2011) 1367–1378. doi:10.1016/j.cma.2010.12.003.
[67] M. D. Alaydin, D. J. Benson, Y. Bazilevs, An updated lagrangian framework for isogeometric kirchhoff–love thin-shell analysis, Computer

Methods in Applied Mechanics and Engineering 384 (2021) 113977.
[68] R. A. Sauer, T. X. Duong, On the theoretical foundations of thin solid and liquid shells, Mathematics and Mechanics of Solids 22 (2017) 343–371.
[69] H. T. McMahon, J. L. Gallop, Membrane curvature and mechanisms of dynamic cell membrane remodelling, Nature 438 (2005) 590–596.
[70] B. Dortdivanlioglu, A. Javili, Plateau Rayleigh instability of soft elastic solids. Effect of compressibility on pre and post bifurcation behavior, Extreme Mechanics Letters 55 (2022) 101797. doi:10.1016/j.eml.2022.101797.
[71] C. Bächer, K. Graessel, S. Gekle, Rayleigh–Plateau instability of anisotropic interfaces. Part 2. Limited instability of elastic interfaces, Journal of Fluid Mechanics 910 (2021) A47. doi:10.1017/jfm.2020.946.